Post-Print

This is the accepted version of:

Completely, partially centralized and fully decentralized control schemes of large adaptive mirrors

Mauro Manetti[a,**], Marco Morandini[a,*], Paolo Mantegazza[a]

[a]*Politecnico di Milano, Department of Aerospace Science and Technology, Via La Masa 34, I-20158 Milano, Italy*

Abstract

Adaptive optics are an increasingly important feature of large ground based telescopes. Large homogeneous deformable secondary mirrors controlled by voice-coil motors, co-located to capacitive position sensors, are a proven working design. Their shape control is mainly based on a completely decentralized high frequency feedback, combined with a low frequency centralized feedforward. This paper investigates the possible improvements achievable through the adoption of partially centralized feedback solutions, comparing their performances with those of fully centralized optimal solutions. The controllers design is based on well known techniques, such as full state linear quadratic regulator, mini-max feedback and independent modal space control.

*Corresponding author
**Now at Microgate Srl, Bolzano, Italy
Email addresses: mauro.manetti@mail.polimi.it (Mauro Manetti), marco.morandini@polimi.it (Marco Morandini), paolo.mantegazza@polimi.it (Paolo Mantegazza)
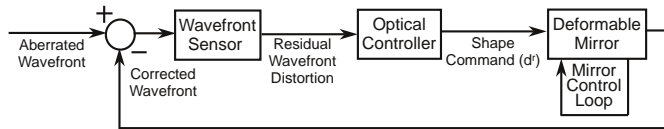
Figure 1: Adaptive optics control system.

1. Introduction

Adaptive optics (AO) corrects image aberrations introduced by atmospheric turbulence (known as seeing), wind disturbances, structural vibrations, thermal deformations, manufacturing and assembly inaccuracies. The main AO components, shown in Fig. 1, are (Hardy, 1998): a wavefront sensor to measure image aberrations from a natural or artificial guide star used as a reference light source, an optimal mirror shape command generator (Optical Controller) to compensate for the deteriorated image wavefront and an actively controlled deformable mirror to compensate the image aberrations by tracking the required optimal mirror shape.

This work focuses on magnetically levitated large deformable mirrors actuated through non contacting voice-coil motors co-located to capacitive position sensors. This technology has been first applied to the Multiple Mirror Telescope (MMT, Wildi et al., 2003) and is at the basis of the Large Binocular Telescope (LBT, Riccardi et al., 2003) AO system, which represents the state of the art (Davies and Kasper, 2012) within the existing working solutions. A similar design is exploited by the Magellan Telescope (MT, Kopon et al., 2010) and will be adopted by the Very Large Telescope (VLT, Biasi et al., 2012), the Giant Magellan Telescope (GMT, Bouchez et al., 2012) and the European Extremely Large Telescope (E-ELT, Gallieni et al., 2009; Biasi and Gallieni, 2011).

Planned secondary deformable mirrors, e.g. VLT-DSM, have dimensions in the order of a meter with more than a thousand actuation points (1170

2

for the VLT-DSM). The required command rates can be up to 2 kHz and the required positioning accuracy, with no externally applied disturbances, is of few nanometers. The control of such stiffness dominated deformable structures represents a real challenge, especially because it is difficult to avoid the excitation of high-frequency structural modes characterized by a high modal density and low damping. The coupling between all the control points, mainly through the mirror stiffness, would suggest the adoption of centralized controllers. Nonetheless the time required to condition, acquire and process all the control signals has imposed the choice of a completely decentralized high frequency feedback (FB), combined with a low frequency centralized feedforward (FF), since the very first realization (MMT, Wildi et al., 2003). Alternative control laws and very different strategies were proposed since the MMT (Grocott and Miller, 1997; Grocott, 1997), see also (Heimsten et al., 2012a,b; Manetti et al., 2010; Manetti, 2011; Ruppel et al., 2013; Stein and Gorinevsky, 2005; Kulkarni et al., 2003; Massioni and Verhaegen, 2009; Ellenbroek et al., 2006). Even so, a completely decentralized FB has been preferred for the MMT, LBT, MT and VLT mirrors. It assured the simplest, yet effective, controller implementation when the MMT system was designed: a single DSP board was able to control a maximum of four actuation points, as it would have been significantly more difficult to accommodate any complete or partial centralization of the high frequency FB contribution. Furthermore experience showed that the FF contribution was essential for achieving the required performances (Brusa-Zappellini et al., 1998).

Future FPGA-based hardware improvements of the aforementioned technology allow to collect an increasing number of controlled points under the same control board, e.g. 16 actuation points for the VLT (Biasi et al., 2012)

and up to 36 actuation points for the E-ELT (Gallieni et al., 2009). This makes the implementation of partially centralized and isolated controller blocks feasible and relatively straightforward, provided they are designed to avoid any data exchange between different control boards.

This paper evaluates and compares the deformable mirror tracking capabilities obtainable with different completely centralized solutions. Since they would be difficult to implement on actual deformable mirrors, these controllers will be used only to assess the behavior of more feasible solutions based on fully and partially decentralized schemes. The design of the aforementioned independent control units will be based on well-known techniques: linear quadratic regulators (LQR), Mini-Max full state feedback and independent modal space control (IMSC). All the controllers are designed with reference to the GMT secondary adaptive mirror, whose performances are computed through high-fidelity system simulations (see Sec. 2). The goal of the work is to estimate the improvements that may be achievable, under the constraint posed by the current hardware, with fully and partially centralized controllers. The comparison should by no means be understood as a definite ranking between centralized and decentralized solutions. In fact, they will confirm that partially decentralized schemes works better than completely decentralized and worse than completely centralized solutions. Although this may seem obvious it was not granted beforehand, because of the peculiar topological limitations imposed by technological implementation constraints. They simply provides a means to estimate and quantify the pros and cons of partially and completely centralized solutions in the face of a complete decentralization for massively controlled shell structures. The results obtained could be of help in driving future design solutions by appropriately assessing the peculiar features of each control scheme.
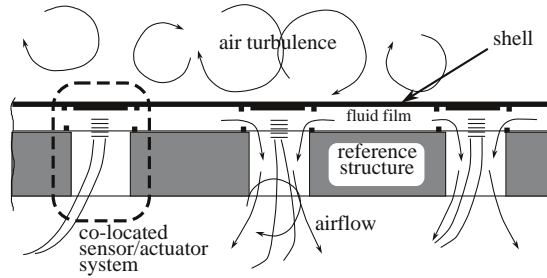
Figure 2: Sketch section of the deformable mirror (Manetti et al., 2010).

2. System simulation

The GMT is a high performance telescope whose segmented primary optics will combine six 8.4 meters off-axis circular mirrors arranged in a hexagonal pattern with a central 8.4 meters mirror (Bouchez et al., 2012). The concave GMT secondary optics has a mirror pattern equal to that of the primary mirror. It should be made of seven 1 m diameter Zerodur mirrors aligned with their seven primary mates, each with 672 actuated points (see Fig. 4), for a total of 4704 actuators. The GMT will adopt the non-contacting adaptive mirror solution (Biasi et al., 2010). Because of the substantial static and dynamic decoupling between the seven secondary mirrors, all the analyses here reported will refer to the on-axis deformable shell alone.

The system model is rather complex and involves a multiphysics description (see Fig. 2) of: the static and dynamic behavior of the deformable mirror, the air squeeze film (30-110 μm) interposed between the mirror and the reference plate, sensors and actuators, the signal A/D/A conversions including quantization errors, noises, delays, and the wind turbulence directly impinging on the mirror surface as an external disturbance. A complete and detailed description of the model, along with numerical/experimental correlations can be found in previous works (Manetti et al., 2010, 2012a,b). .

In the followings just a short summary of the system model is presented.

The main aim of such a detailed model is the development of an accurate simulator and not a system description suitable for the control design. Despite this fact an approximation scheme can be exploited to suggest and verify reduced order models that are more suitable for a controller design (see Sec. 4.).

The mirror structural dynamics are described through the development of a shell Finite Element (FE) model, which is condensed by exploiting normal vibration modes up to a sufficiently high frequency of 32 kHz. The $(n_g \times 1)$ vector of FE nodal out of plane displacements $\boldsymbol{x}$ is approximated as $\boldsymbol{x} = \boldsymbol{X}_g \boldsymbol{q}$, with $\boldsymbol{q}$ being the $(n_m \times 1)$ vector of the modal generalized coordinates and $\boldsymbol{X}_g$ the $(n_g \times n_m)$ modal shape matrix. Assuming a unit modal mass normalization and a diagonal modal damping, the ith modal equation can be written as

$$\ddot{q}_i + 2\xi_i\omega_i\dot{q}_i + \omega_i^2 q_i = f_{m_i}^c + f_{m_i}^t + f_{m_i}^f, \tag{1}$$

where q_i is the ith modal coordinate, while ξ_i and ω_i are, respectively, the modal damping coefficient and natural frequency. The modal force is the sum of three $(n_m \times 1)$ vectors: the control forces $\boldsymbol{f}_m^c = \boldsymbol{X}^T \text{sat}(\boldsymbol{f}_a^c)$, the air turbulence disturbance $\boldsymbol{f}_m^t = \boldsymbol{X}^T \boldsymbol{f}_a^t$ and the fluid film generalized forces $\boldsymbol{f}_m^f = \boldsymbol{X}_f^T \boldsymbol{f}_a^f$. The $(n_a \times n_m)$ matrix $\boldsymbol{X}$ samples the modal shapes at the actuation points, $\boldsymbol{X}_f$ samples the modal shapes at the fluid dynamic nodes, while the operator sat() accounts for actuator saturations.

A simplified turbulence disturbance approximation is proposed in (Manetti et al., 2012a); within the present work the disturbance is considered fully correlated over the mirror surface and the turbulence velocity time history is obtained through a first order rational approximation of its von Karman power spectrum. The Gemini Telescope experimental measurements (Smith, 2001) suggest a turbulence average velocity of 7.5 m/s and a velocity standard

deviation of 2 m/s.

The voice-coil forces are assumed to be ideally pointwise and acting normally to the deformable mirror. The actuators dynamics are described by means of an uncoupled first order model

$$\dot{\boldsymbol{x}}_f = -\lceil\diagdown\boldsymbol{\omega}_f\diagup\rceil\boldsymbol{x}_f + \lceil\diagdown\boldsymbol{\omega}_f\diagup\rceil\boldsymbol{f}^c, \tag{2}$$

$$\boldsymbol{f}_a^c = \boldsymbol{x}_f,$$

where $\boldsymbol{f}^c$ represents the $(n_a \times 1)$ required control forces vector, while $\lceil\diagdown\boldsymbol{\omega}_f\diagup\rceil$ is an $(n_a \times n_a)$ diagonal matrix with ω_f the circular corner frequency of the actuators dynamics.

The capacitive sensors provides an approximately co-located measurement of the shell displacement at each actuation point. Their dynamics can be described, just like that of the actuators, as

$$\dot{\boldsymbol{x}}_p = -\lceil\diagdown\boldsymbol{\omega}_s\diagup\rceil\boldsymbol{x}_p + \lceil\diagdown\boldsymbol{\omega}_s\diagup\rceil\boldsymbol{d}, \tag{3}$$

$$\boldsymbol{p} = \boldsymbol{x}_p,$$

where $\boldsymbol{p}$ represents the $(n_a \times 1)$ vector of measured positions, $\boldsymbol{d} = \boldsymbol{X}\boldsymbol{q}$ is the $(n_a \times 1)$ vector of ideal control points displacement and the $(n_a \times n_a)$ diagonal matrix $\lceil\diagdown\boldsymbol{\omega}_s\diagup\rceil$ contains the sensors dynamics circular corner frequency ω_s. The non ideal co-location of the sensors can be accounted for as well (Manetti et al., 2012b).

The fluid film interposed between the mirror and the reference plane, whose thickness can vary within the range of 30-120 μm, strongly affects the mirror dynamics, especially its damping. Hence a reasonable model of its effects is mandatory to obtain a realistic prediction of the system stability and performances. The simulator includes a fluid dynamics description which exploits an ad hoc two dimensional formulation based on a finite volume discretization of the Navier-Stokes equations (Manetti et al., 2012a).

7

Its coupling to the structural motion is obtained through the interpolation provided by $\boldsymbol{X}_f$.

3. Control strategies

The deformable mirror controller continuously adjusts the mirror surface shape to compensate the residual optical aberrations measured by the wavefront sensor. The desired mirror shape is computed by the optimal mirror shape commad generator. The mirror controller receives the kth shape update as a $(n_a \times 1)$ step command vector, $\boldsymbol{d}^r_{(k)}$, at a relatively low command frequency (250-2000 Hz) (see Fig. 1). Each step command is usually shaped in time through appropriate smoothing functions, $f_{sh}(t)$, e.g. a fifth order polynomial. Each command step can thus be split in a first time varying part followed by a steady position, as shown in Fig. 3. The $(n_a \times 1)$ reference position vector has to be tracked in time at each actuation point and can be written as

$$\boldsymbol{d}^r(t) = \boldsymbol{d}^r_{(k)} + (\boldsymbol{d}^r_{(k+1)} - \boldsymbol{d}^r_{(k)})f_{sh}(t), \tag{4}$$

thus determining the reference position $\boldsymbol{d}^r(t)$ at each time step with a single multiply/add instruction and also allowing to simply scale the FF action. Such a solution is preferred because it avoids a more expensive step-by-step computation associated to a high order low-pass filtering, while providing an equivalent smoothing action of the command signal.

The already working solutions are based on a completely decentralized proportional-derivative feedback, combined with a feedforward contribution (Brusa-Zappellini et al., 1998). So the control force vector can be written as

$$\boldsymbol{f}^c = \boldsymbol{f}^c_f + \boldsymbol{f}^c_d, \tag{5}$$

where the $(n_a \times 1)$ vectors $\boldsymbol{f}^c_f$ and $\boldsymbol{f}^c_d$ are respectively the FB and FF forces. The system positioning error required by the FB proportional action is di-

8
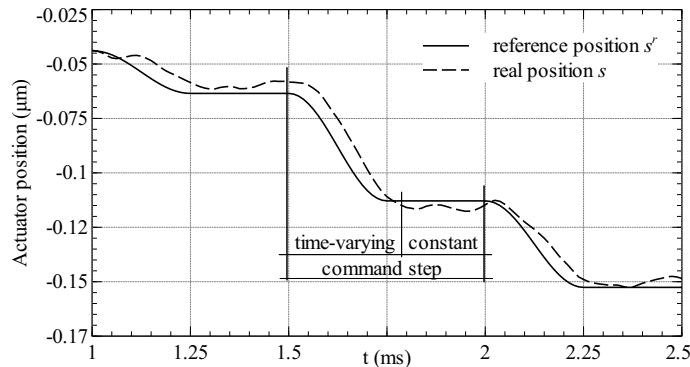
Figure 3: Sketch of typical command steps split into a time varying and steady part (Manetti et al., 2010).

rectly obtained through capacitive sensors measurements, while the mirror velocity is estimated through appropriate pseudo-derivative filters applied to the position measure, without the need of any observer or more general compensator. The FB control is realized digitally at a relatively high control frequency (70-100 kHz). The FF is applied at the same frequency, but it is computed at the lower command frequency, making it feasible a fully centralized FF. An improved controller has been proposed in (Manetti et al., 2010), where the FF was modified, while the completely decentralized FB structure was left untouched. A brief summary of the FF and FB terms of this scheme can be found in Subsecs. 3.1, 3.2.

In the following parts of this paper the performances achievable through the application of high frequency fully centralized and partially decentralized FB solutions are compared with those of the existing completely decentralized implementation. Once more, it should be remarked that a complete centralization remains unfeasible without a complete rework of the existing hardware technology. It is nevertheless assumed as a reference, providing a good performance comparison benchmark for all the other methods. Partial decentralization is an already viable strategy because new systems are
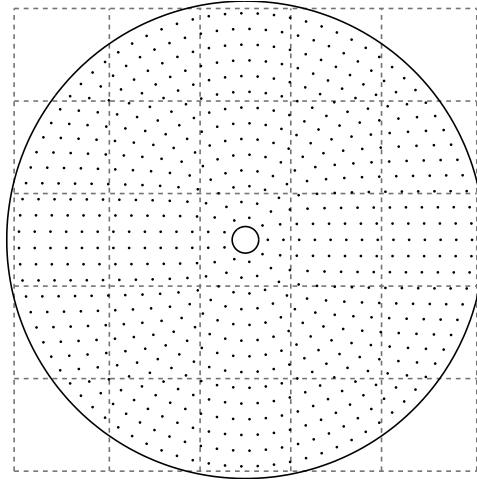
Figure 4: Actuators layout of the on-axis GMT secondary mirror with the related (5×5) square grid subdivision.

equipped with FPGA-based control boards handling up to 36 control points each. It is however still difficult to exchange data between different control boards at the high FB control frequency. This limits the feasible structure of any partially centralized FB, that cannot couple different actuators blocks. These actuators blocks are here simulated by partitioning the control points with a (5×5) square grid, as shown in Fig. 4.

The above leads to 25 independent blocks, with a maximum of 37 and an average of 27 control points per block. An additional constraint comes from the need of avoiding the introduction of any full system observer/compensator. The only available measures are the control points position and locally estimated velocity; these are the only informations that are supposed to be required by the controller, just like for the already working units. By adhering to the two aforementioned constraints the solutions proposed in this paper can be applied to actual systems without the need of any hardware change.

The controllers are designed using well established control techniques:
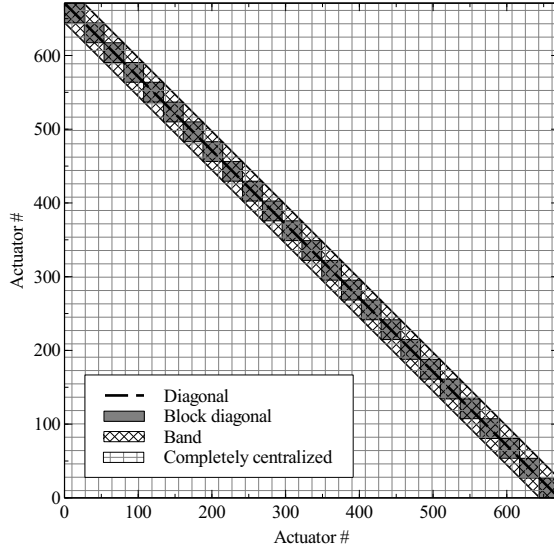
Figure 5: Different gain matrix structures, which can be achieved through different control design implementations: completely decentralized (diagonal), partially decentralized (block diagonal), partially centralized (band), completely centralized.

LQR (see Subsec. 3.3), Mini-Max full state feedback (see Subsec. 3.4) and independent modal space control (see Subsec. 3.5). All these control techniques are applied to the above mentioned three possible control structures, i.e. the completely decentralized (diagonal), the partially decentralized (block diagonal) and the completely centralized topologies of Fig. 5; a more classic band topology is considered as well, as it allows to evaluate the effectiveness of the block diagonal implementation.

Almost all the analyses are performed by leaving the enhanced FF contribution of Subsec. 3.1 unchanged; a single analysis is carried out without any FF, so to well highlight its importance in obtaining satisfactory performances for a stiffness dominated system.

3.1. Feedforward contributions

The $(n_a \times 1)$ FF force vector, $\boldsymbol{f}_f^c$, can be split in two main contributions

$$\boldsymbol{f}_f^c = \boldsymbol{f}_{fs}^c + \boldsymbol{f}_{fd}^c, \tag{6}$$

11

where $\boldsymbol{f}_{fs}^c$ is the $(n_a \times 1)$ static FF term, while $\boldsymbol{f}_{fd}^c$ is the $(n_a \times 1)$ dynamic FF term. The static FF represents the static forces required to obtain the commanded shape and it is based on the $(n_a \times n_a)$ experimentally identified stiffness matrix $\boldsymbol{K}^*$ (see (Manetti et al., 2010) for more details),

$$\boldsymbol{f}_{fs}^c(t) = \boldsymbol{K}^*\boldsymbol{d}^r(t), \tag{7}$$

where $\boldsymbol{d}^r(t)$, defined in Eq. 4, is computed with the the same shaping function $f_{sh}(t)$ used to define the reference position vector. While the MMT, LBT and MT mirrors were built using a different shaping function for the static FF term, this is no more the case since the introduction of the dynamic FF with the VLT mirror. The stiffness matrix is fully populated. Thus the static FF is a completely centralized contribution. The computation of the static FF term, Eq. 7, can be easily modified to introduce a sort of very effective and efficient integral FB together with the static FF itself (Manetti et al., 2010, 2013). This allows to increase the system robustness with respect to external disturbances and can well fix possible inaccuracies of the identified matrix $\boldsymbol{K}^*$. All the results that will be presented are obtained with the use of this modification.

The dynamic FF is meant to compensate for the system dynamics and improves its performances during the transient part of each command step. The $(n_a \times 1)$ vector, $\boldsymbol{f}_{fd}^c$, is computed as

$$\boldsymbol{f}_{fd}^c(t) = \boldsymbol{M}^*\ddot{\boldsymbol{d}}^r(t) + \boldsymbol{C}^*\dot{\boldsymbol{d}}^r(t), \tag{8}$$

where the $(n_a \times 1)$ vector $\ddot{\boldsymbol{d}}$ is the tracking reference acceleration, while the $(n_a \times 1)$ vector $\dot{\boldsymbol{d}}$ is the tracking reference velocity. The $(n_a \times n_a)$ matrices $\boldsymbol{M}^*$ and $\boldsymbol{C}^*$ should represent the system damping and mass, lumped at the actuation points. Such matrices can be identified with a procedure similar to that used to obtain $\boldsymbol{K}^*$ (Manetti, 2011); nevertheless it is shown in (Manetti

et al., 2010) that they can be proficiently approximated as being diagonal through two scalar terms m and c, i.e. $\boldsymbol{M}^* = \lceil\searrow m\searrow\rfloor$ and $\boldsymbol{C}^* = \lceil\searrow c\searrow\rfloor$. In this way their dynamic contributions become completely decentralized. The dynamic FF is applied at the high control frequency, but computed at the lower command rate, just like the static FF term.

3.2. Completely decentralized PD control

The control solution proposed in (Manetti et al., 2010) suggests the implementation of a completely decentralized PDD2 controller; here, we limit ourselves to a simpler and more standard PD controller, so that the $(n_a \times 1)$ FB control vector can be written as

$$\boldsymbol{f}_d^c(t) = \lceil\searrow\boldsymbol{G}_d\searrow\rfloor\left(\dot{\boldsymbol{d}}^r(t) - \dot{\boldsymbol{p}}(t)\right) + \lceil\searrow\boldsymbol{G}_p\searrow\rfloor\left(\boldsymbol{d}^r(t) - \boldsymbol{p}(t)\right), \tag{9}$$

where the $(n_a \times n_a)$ diagonal matrices $\lceil\searrow\boldsymbol{G}_d\searrow\rfloor$ and $\lceil\searrow\boldsymbol{G}_p\searrow\rfloor$ are the derivative and proportional gains. The $(n_a \times 1)$ vector of the measured control point velocities, $\dot{\boldsymbol{p}}$, is estimated through first-order pseudo-derivative filters. Their state space realization is

$$\dot{\boldsymbol{x}}_v = -\lceil\searrow\boldsymbol{\omega}_v\searrow\rfloor\boldsymbol{x}_v + \lceil\searrow\boldsymbol{\omega}_v\searrow\rfloor\boldsymbol{p}, \tag{10}$$

$$\boldsymbol{v}_p = -\lceil\searrow\boldsymbol{\omega}_v\searrow\rfloor\boldsymbol{x}_v + \lceil\searrow\boldsymbol{\omega}_v\searrow\rfloor\boldsymbol{p},$$

with $\lceil\searrow\boldsymbol{\omega}_v\searrow\rfloor$ a constant diagonal matrix based on the scalar value ω_v, which represents the pseudo-derivative filter corner frequency. The output vector $\boldsymbol{v}_p$ can be used to approximate $\dot{\boldsymbol{p}}$ in Eq. 9 and wherever the time derivative of the measured position may be required in the following part of the paper.

3.3. LQR control

Consider a standard, asymptotically stable, linear time invariant state space system representation:

$$\dot{\boldsymbol{x}} = \boldsymbol{A}\boldsymbol{x} + \boldsymbol{B}\boldsymbol{u}. \tag{11}$$

The optimal linear quadratic regulator (LQR) guarantees the obtainement a unique, stable time invariant control solution through a full state proportional algebraic regulator $\boldsymbol{u} = -\boldsymbol{G}\boldsymbol{x}$, by minimizing the functional

$$J(\boldsymbol{u}) = \frac{1}{2} \int_0^\infty \left(\boldsymbol{x}^T \boldsymbol{Q} \boldsymbol{x} + \boldsymbol{u}^T \boldsymbol{R} \boldsymbol{u} \right) dt, \tag{12}$$

where the time invariant weighting matrices $\boldsymbol{Q}$ and $\boldsymbol{R}$ are respectively at least semidefinite positive symmetric and definite positive symmetric.

A proper choice of the system model, Eq. 11, is crucial in providing a good control design. Thus, we assume here that the nominal plant can be approximated through three $(n_a \times n_a)$ matrices, $\boldsymbol{M}$, $\boldsymbol{C}$ and $\boldsymbol{K}$, which represent, respectively, the system mass, damping and stiffness matrices condensed at the actuation points. These matrices can be interpreted as an approximated reduced order model of both the system structural and fluid dynamics behavior. Different ways to retrieve these matrices can be found in Sec. 4, along with a discussion about the limitations of such a simplified system description. Once $\boldsymbol{M}$, $\boldsymbol{C}$ and $\boldsymbol{K}$ are identified, the nominal system state space model can be represented either as a second order model in the physical coordinates

$$\boldsymbol{M}\ddot{\boldsymbol{p}} + \boldsymbol{C}\dot{\boldsymbol{p}} + \boldsymbol{K}\boldsymbol{p} = \boldsymbol{u} \tag{13}$$

or by defining the following matrices of the corresponding state representation of Eq 11 (e.g. Géradin and Rixen, 1997)

$$\boldsymbol{A} = \begin{bmatrix} \boldsymbol{0} & \boldsymbol{I} \\ -\boldsymbol{M}^{-1}\boldsymbol{K} & -\boldsymbol{M}^{-1}\boldsymbol{C} \end{bmatrix}, \boldsymbol{B} = \begin{bmatrix} \boldsymbol{0} \\ \boldsymbol{M}^{-1} \end{bmatrix}, \tag{14}$$

where $\boldsymbol{A}$ is the $(2n_a \times 2n_a)$ state space matrix and $\boldsymbol{B}$ is the $(2n_a \times n_a)$ state space input matrix. The $(2n_a \times 1)$ state vector $\boldsymbol{x}$ is now $\boldsymbol{x}^T = \begin{bmatrix} \boldsymbol{p}^T & \dot{\boldsymbol{p}}^T \end{bmatrix}$, while the $(n_a \times 1)$ input vector represents the mirror FB control forces, $\boldsymbol{u} = \boldsymbol{f}_d^c$. Now, once an appropriate $(2n_a \times 2n_a)$ weighting matrix $\boldsymbol{Q}$ and a $(n_a \times n_a)$

14

matrix $\boldsymbol{R}$ have been chosen, the $(n_a \times 2n_a)$ optimal feedback gain matrix $\boldsymbol{G}$ can be computed by solving an algebraic Riccati equation (ARE). The gain matrix can be partitioned as $\boldsymbol{G} = [\boldsymbol{G}_p\, \boldsymbol{G}_d]$, where the $(n_a \times n_a)$ matrices $\boldsymbol{G}_p$ and $\boldsymbol{G}_d$ can be interpreted as the centralized proportional and derivative optimal gains obtained through the LQR design. The system FB contribution

$$\boldsymbol{f}_d^c(t) = -\boldsymbol{G}\tilde{\boldsymbol{x}} = \boldsymbol{G}_p\left(\boldsymbol{d}^r - \boldsymbol{p}\right) + \boldsymbol{G}_d\left(\dot{\boldsymbol{d}}^r - \dot{\boldsymbol{p}}\right) \tag{15}$$

requires a completely centralized computation; the vectors $\boldsymbol{p}$ and $\dot{\boldsymbol{p}}$ are the same data needed for the completely decentralized solution of Eq. 9, and $\dot{\boldsymbol{p}}$ is estimated with the pseudo-derivative filters of Eq. 10.

A distributed control structure based on the FB of Eq. 15 should not require any data exchange between the different DSP boards, as explained in Sec. 3, so constraining the structure of matrices $\boldsymbol{G}_p$ and $\boldsymbol{G}_d$. The proposed solution is straightforward and very intuitive from an engineering point of view. It is based on the idea of removing from the system nominal plant model all the coupling elements between actuated points belonging to different DSP control boards. The matrices can thus be partitioned and reassembled through n^{dsp} uncoupled blocks matrices, $\boldsymbol{K} = \left[\diagdown\overline{\boldsymbol{K}}_i\diagdown\right]$, $\boldsymbol{C} = \left[\diagdown\overline{\boldsymbol{C}}_i\diagdown\right]$ and $\boldsymbol{M} = \left[\diagdown\overline{\boldsymbol{M}}_i\diagdown\right]$, where n^{dsp} is the number of DSP control boards. The notation $\left[\diagdown\bullet\diagdown\right]$ stands for a (block-) diagonal matrix, index i ranges from 1 to n^{dsp} and the ith block matrices $\overline{\boldsymbol{K}}_i$, $\overline{\boldsymbol{C}}_i$ and $\overline{\boldsymbol{M}}_i$ have dimension $(n_i^{block} \times n_i^{block})$, with n_i^{block} equal to the number of actuation points handled by the ith DSP control board. The solution of the original LQR design is thus recast into the solution of n^{dsp} smaller independent problems. As a direct consequence, the proportional and derivative gain matrices $\boldsymbol{G}_p$ and $\boldsymbol{G}_d$ assume the same block diagonal structure of the modified system matrices, $\boldsymbol{G}_p = \left[\diagdown\overline{\boldsymbol{G}}_i\diagdown\right]$ and $\boldsymbol{G}_d = \left[\diagdown\overline{\boldsymbol{G}}_{d_1}\diagdown\right]$. The resulting FB control is centralized within only the actuators belonging to each DSP unit, and there is no need to exchange any

information between different control boards.

The deletion of some coupling terms from the system matrices leads to a block diagonal system approximation and could be justified because the larger is the distance between different control points the smaller is their coupling. This may not completely justify the proposed approach. As a matter of fact not only the coupling between distant actuators is neglected, but also that of the actuation points that are close to each other but handled by different DSPs. However, the system condensed mass and damping matrices have a strong diagonal dominance, as shown in (Manetti et al., 2010; Manetti, 2011). For this reason the suggested block diagonal representation is likely to provide an adequate approximation of the system dynamics. The block diagonal approximation of the stiffness matrix K negatively affects the description of the system static response, that would be otherwise exact with a fully populated stiffness matrix. The static positioning accuracy is nevertheless well guaranteed by the FF contribution. Note that an alternative procedure for designing the block-diagonal and diagonal controllers could be to constrain the structure of the gain matrix, still exploiting the fully populated system matrices M, C and K. This approach leads to a non convex, constrained, optimization problem, that can be solved, starting from and maintaining a stable solution, with a numerical optimization (e.g. Mercadal, 1991; Ercoli Finzi et al., 1985). However, although the resulting solution would provide better performance, the problem at hand proved to be too large to be efficiently solved numerically.

3.4. Mini-Max full state feedback control

As just stated, the nominal plant used for the design of the LQR controller is an acceptable approximation, but by no means an accurate description of the actual system. It lacks, among other things, a description of the high

frequency system fluid-structural dynamics, of the sensor and actuator dynamics, of the pseudo-derivative filters, and of control system delays. The Mini-Max controller adds an additional degree of freedom to guarantee robustness in presence of unmodeled uncertainties, and allows to compromise between the optimal performances of the LQR control and the robust design provided by the introduction of a worst disturbance $\boldsymbol{v}(t)$ acting on the system (Lublin and Athans, 2010):

$$\dot{\boldsymbol{x}} = \boldsymbol{A}\boldsymbol{x} + \boldsymbol{B}\boldsymbol{u} + \boldsymbol{L}\boldsymbol{v}, \tag{16}$$

where the $(2n_a \times n_a)$ matrix $\boldsymbol{L} = \boldsymbol{B}$ defines how the disturbance vector $\boldsymbol{v}$ affects the system dynamics. The aim is to exploit an optimal control solution, which is capable to reject the effect of disturbances, so that a more robust design can be obtained. The idea is to include the determination of the worst possible disturbance into the quadratic cost functional. Therefore, the infinite horizon performances are degraded by setting

$$J(\boldsymbol{u}, \boldsymbol{v}) = \frac{1}{2} \int_0^\infty \left(\boldsymbol{x}^T \boldsymbol{Q} \boldsymbol{x} + \boldsymbol{u}^T \boldsymbol{R} \boldsymbol{u} - \gamma^2 \boldsymbol{v}^T \boldsymbol{v} \right) dt, \tag{17}$$

with γ a positive parameter. The design goal is the minimization of the functional $J(\boldsymbol{u}, \boldsymbol{v})$ with respect to the control unknowns $\boldsymbol{u}$, while maximizing it with respect to $\boldsymbol{v}$. This is a typical differential game Mini-Max optimization problem, $\min_{\boldsymbol{u}} \max_{\boldsymbol{v}} J(\boldsymbol{u}, \boldsymbol{d})$, i.e. an effort to find the optimal control in presence of the worst admissible disturbances. The solution is not guaranteed to exist for any positive γ, but when it does a full state control law is obtained. Consider an asymptotically stable system and assume that the state vector $\boldsymbol{x}$ is available and the disturbance $\boldsymbol{v}$ is bounded. If the optimal value of $J(\boldsymbol{u}, \boldsymbol{d})$ constrained by Eq. 16 exists, then it is a unique saddle point with the optimal Mini-Max control law given by

$$\boldsymbol{u} = -\boldsymbol{G}\boldsymbol{x}, \qquad \boldsymbol{G} = \boldsymbol{R}^{-1}\boldsymbol{B}^T\boldsymbol{P}, \tag{18}$$

the worst disturbance being:

$$v = \frac{1}{\gamma^2} \boldsymbol{L}^T \boldsymbol{P} \boldsymbol{x}. \tag{19}$$

The matrix $\boldsymbol{P}$ is the unique, symmetric, at least positive semidefinite solution of the matrix Riccati Equation

$$\boldsymbol{P}\boldsymbol{A} + \boldsymbol{A}^T \boldsymbol{P} - \boldsymbol{P}\left(\boldsymbol{B}\boldsymbol{R}^{-1}\boldsymbol{B}^T - \frac{1}{\gamma^2}\boldsymbol{L}\boldsymbol{L}^T\right)\boldsymbol{P} + \boldsymbol{Q} = \boldsymbol{0}. \tag{20}$$

When the optimization problem solution exists then the resulting closed-loop system, $\dot{\boldsymbol{x}} = (\boldsymbol{A} - \boldsymbol{B}\boldsymbol{G})\,\boldsymbol{x}$, is guaranteed to be asymptotically stable. Of course the system disturbances are unknown by definition, so the optimal feedback based on them, Eq. 19, cannot be applied. However the resulting Mini-Max controller provides a closed loop stable system $\dot{\boldsymbol{x}} = \left(\boldsymbol{A} + \gamma^{-2}\boldsymbol{L}\boldsymbol{L}^T\boldsymbol{P} - \boldsymbol{B}\boldsymbol{G}\right)\boldsymbol{x}$ for which it is possible to prove that, after removing the worst disturbance feedback, i.e. $\gamma^{-2}\boldsymbol{L}\boldsymbol{L}^T\boldsymbol{P}$, the final solution not only remains stable, but its stability margin is improved (Colaneri et al., 1997). This point of view indicates that the optimal control gain matrix $\boldsymbol{G}$ is designed on the penalized system $\dot{\boldsymbol{x}} = \left(\boldsymbol{A} + \gamma^{-2}\boldsymbol{L}\boldsymbol{L}^T\boldsymbol{P}\right)\boldsymbol{x} = (\boldsymbol{A} + \Delta\boldsymbol{A}_w)\,\boldsymbol{x}$ and then applied to the nominal system. Because γ drives the negative term of the ARE equation, $\gamma^{-2}\boldsymbol{L}\boldsymbol{L}^T$, there is a minimum positive value γ_{min} below which the Riccati equation cannot be solved or the matrix $\boldsymbol{P}$ does not result positive semidefinite. Useful γ values lies within the range $[\gamma_{min}, \infty]$. The solution will tend to the LQR design, for which Eq. 18 still applies, as $\gamma \to \infty$. At γ_{min} the so called full information H^∞ controller is obtained.

The Mini-Max feedback action is computed as a function of the tracking error $\tilde{\boldsymbol{x}}$, as for the LQR control, and the control contribution assumes exactly the same structure as Eq. 15. The distributed control is built by following the same procedure suggested for the LQR control, leading to n^{dsp} smaller in-

dependent design problems, hence to uncoupled block diagonal proportional and derivative gain matrices.

3.5. Independent modal space control (IMSC)

Normal vibration modes can be exploited not only to describe the structural behavior, as seen in Sec. 2, but also to approach the control of deformable structures. Designing the controller in the modal space is appealing, since it allows addressing the system dynamics as a set of independent second order equations, so that the controller design can be applied to uncoupled nominal plants that are drastically reduced in size. This allowed modeling the sensor and actuator dynamics and the pseudo-derivative filters, still obtaining a set of independent nominal plants with reasonable dimensions. Moreover a modal control naturally introduces the capability to tune the system behavior in the frequency domain, and in the adaptive optics field the deformable mirror specifications in terms of performances are often provided in a more comfortable way in terms of modal response specifications.

Using normal vibration modes the nominal plant for the controller design can be written as

$$\ddot{\boldsymbol{\eta}} + \left[\diagdown 2\boldsymbol{\omega}_c \boldsymbol{\xi}_c \diagdown \right] \dot{\boldsymbol{\eta}} + \left[\diagdown \boldsymbol{\omega}_c^2 \diagdown \right] \boldsymbol{\eta} = \boldsymbol{u}_m, \tag{21}$$

where $\boldsymbol{\eta}$ is the $(\overline{n}_m \times 1)$ vector of the controlled modal amplitudes, $\boldsymbol{u}_m$ is the $(\overline{n}_m \times 1)$ vector of the modal control forces, while $\left[\diagdown 2\boldsymbol{\omega}_c \boldsymbol{\xi}_c \diagdown \right]$ and $\left[\diagdown \boldsymbol{\omega}_c^2 \diagdown \right]$ are the $(\overline{n}_m \times \overline{n}_m)$ diagonal matrices representing the modal damping and stiffness. The $\overline{n}_m$ natural frequencies $\boldsymbol{\omega_c}$ can be obtained, along with their corresponding mode shapes, from the same accurate FE model of Sec. 2. On the contrary, the $\overline{n}_m$ modal damping coefficients $\boldsymbol{\xi}_c$ should approximate both the structural and the fluid film damping. Further details about this modal representation can be found in Sec. 4. A major advantage of the modal representation is its capability of reducing the system to a set of $\overline{n}_m$ uncoupled

19

equations. A straightforward way to modify the system dynamics, while preserving its uncoupled representation, is the introduction of a completely diagonal proportional-derivative modal feedback: $\boldsymbol{u}_m = -\left\lceil\!\!\searrow\!\boldsymbol{G}_p^m\!\searrow\!\right\rfloor\boldsymbol{\eta} - \left\lceil\!\!\searrow\!\boldsymbol{G}_d^m\!\searrow\!\right\rfloor\dot{\boldsymbol{\eta}}$, where $\left\lceil\!\!\searrow\!\boldsymbol{G}_p^m\!\searrow\!\right\rfloor$ and $\left\lceil\!\!\searrow\!\boldsymbol{G}_d^m\!\searrow\!\right\rfloor$ are respectively the proportional and derivative $(\overline{n}_m \times \overline{n}_m)$ diagonal modal gain matrices. This solution is usually called independent modal space control (IMSC) (Meirovitch, 1990). The IMSC requires the measurement of modal amplitudes and the application of modal forces. However the system here considered relies on a finite number of discrete sensors and actuators. It is thus mandatory to find a relationship between the modal and the physical space.

The capacitive sensors measurement of the positions, $\boldsymbol{p}$, can be approximated through a truncated modal basis as $\boldsymbol{p} = \boldsymbol{X}_c\boldsymbol{\eta}$, where $\boldsymbol{X}_c$ is the $(n_a \times \overline{n}_m)$ matrix sampling the controlled modal shapes at the controlled points. If the number of controlled modes, $\overline{n}_m$, is chosen equal to the number of controlled points, n_a, the inverse relation could be easily obtained as $\boldsymbol{\eta} = \boldsymbol{X}_c^{-1}\boldsymbol{p}$. The computation of $\boldsymbol{X}_c^{-1}$ requires that at least n_a modal shapes are observable. The system modal shapes observability can be easily checked, through the procedure suggested in (Manetti et al., 2010), by exploiting the Hankel singular values of the Gramian matrices (Gawronsky, 2004). The Hankel singular values usually show that more than n_a modal shapes result observable for the sensors layout of the here considered deformable mirrors. However, experience suggests that the degree of observability decreases for increasing natural frequencies. This can lead to numerical problems in the computation of the inverse matrix $\boldsymbol{X}_c^{-1}$, which would have several hundreds or thousands rows for the latest generation mirrors. Moreover the number of controlled modes can hardly equal the number of controlled points because the spillover control action would easily endanger system stability. These

practical reasons suggest to choose $\overline{n}_m < n_a$ and exploit the Moore–Penrose pseudo-inverse $\boldsymbol{X}_c^\dagger$ of matrix $\boldsymbol{X}_c$, $\boldsymbol{X}_c^\dagger = \left(\boldsymbol{X}_c^T \boldsymbol{X}_c\right)^{-1} \boldsymbol{X}_c^T$, to obtain the modal amplitudes from the position measurements (Meirovitch and Baruh, 1985):

$$\boldsymbol{\eta} = \boldsymbol{X}_c^\dagger \boldsymbol{p}. \tag{22}$$

The same pseudo–inverse matrix can be used to evaluate the modal velocities, $\dot{\boldsymbol{\eta}} = \boldsymbol{X}_c^\dagger \dot{\boldsymbol{p}}$.

A related problem is the determination of a relation between modal control forces and actuators forces. It is well known (e.g. Géradin and Rixen, 1997) that the generalized control forces can be expressed as $\boldsymbol{u}_m = \boldsymbol{X}_c^T \boldsymbol{f}_d^c$. The Moore-Penrose pseudo-inverse $\boldsymbol{X}_c^{T\dagger} = \boldsymbol{X}_c \left(\boldsymbol{X}_c^T \boldsymbol{X}_c\right)^{-1}$ allows to find the minimum norm solution

$$\boldsymbol{f}_d^c = \boldsymbol{X}_c^{T\dagger} \boldsymbol{u}_m. \tag{23}$$

The modal FB force vector of Eq. 21 can be rewritten as

$$\begin{aligned}
\boldsymbol{u}_m &= \boldsymbol{X}_c^T \boldsymbol{f}_d^c \\
&= \boldsymbol{X}_c^T \boldsymbol{X}_c^{T\dagger} \left(- \left\lceil \diagdown \boldsymbol{G}_p^m \diagdown \right\rfloor \boldsymbol{\eta} - \left\lceil \diagdown \boldsymbol{G}_d^m \diagdown \right\rfloor \dot{\boldsymbol{\eta}}\right) \\
&= - \left(\left\lceil \diagdown \boldsymbol{G}_p^m \diagdown \right\rfloor \boldsymbol{X}_c^\dagger \boldsymbol{p} + \left\lceil \diagdown \boldsymbol{G}_d^m \diagdown \right\rfloor \boldsymbol{X}_c^\dagger \dot{\boldsymbol{p}}\right), \tag{24}
\end{aligned}$$

where the property $\boldsymbol{X}_c^T \boldsymbol{X}_c^{T\dagger} = \boldsymbol{I}$ has been exploited. This is a crucial point for preserving the uncoupled structure of the modal control problem. A further improvement of the plant modeling accuracy can be obtained by introducing the actuators and sensors dynamics, Eqs. 2 and 3, into Eq. 24, together with the pseudo-derivative filter action, Eq. 10. For convenience

this operation is performed in the Laplace domain

$$\mathcal{L}(\boldsymbol{u}_m) = -\boldsymbol{X}_c^T \left[\diagdown \frac{\boldsymbol{\omega}_a}{\boldsymbol{s}+\boldsymbol{\omega}_a} \diagdown \right] \boldsymbol{X}_c^{T\dagger}$$
$$\begin{pmatrix} \left[\diagdown \boldsymbol{G}_p^m \diagdown \right] \boldsymbol{X}_c^{\dagger} \left[\diagdown \frac{\boldsymbol{\omega}_s}{\boldsymbol{s}+\boldsymbol{\omega}_s} \diagdown \right] \boldsymbol{d} + \\ \left[\diagdown \boldsymbol{G}_d^m \diagdown \right] \boldsymbol{X}_c^{\dagger} \left[\diagdown \frac{\boldsymbol{\omega}_v \boldsymbol{s}}{\boldsymbol{s}+\boldsymbol{\omega}_v} \diagdown \right] \left[\diagdown \frac{\boldsymbol{\omega}_s}{\boldsymbol{s}+\boldsymbol{\omega}_s} \diagdown \right] \boldsymbol{d} \end{pmatrix} \quad (25)$$

where s is the Laplace variable, while the $(n_a \times n_a)$ constant diagonal matrices $\left[\diagdown \frac{\boldsymbol{\omega}_a}{\boldsymbol{s}+\boldsymbol{\omega}_a} \diagdown \right]$, $\left[\diagdown \frac{\boldsymbol{\omega}_s}{\boldsymbol{s}+\boldsymbol{\omega}_s} \diagdown \right]$ and $\left[\diagdown \frac{\boldsymbol{\omega}_v \boldsymbol{s}}{\boldsymbol{s}+\boldsymbol{\omega}_v} \diagdown \right]$ represent respectively the transfer functions of the actuators dynamics, sensors dynamics and pseudo-derivative filter action. These constant diagonal matrices act as frequency dependent scalar coefficients of the modal control forces, so that Eq. 25 can be equivalently rewritten as

$$\mathcal{L}(\boldsymbol{u}_m) = -\left[\diagdown \frac{\boldsymbol{\omega}_a}{\boldsymbol{s}+\boldsymbol{\omega}_a} \diagdown \right] \left[\diagdown \frac{\boldsymbol{\omega}_s}{\boldsymbol{s}+\boldsymbol{\omega}_s} \diagdown \right]$$
$$\left(\left[\diagdown \boldsymbol{G}_p^m \diagdown \right] \boldsymbol{\eta} + \left[\diagdown \frac{\boldsymbol{\omega}_v \boldsymbol{s}}{\boldsymbol{s}+\boldsymbol{\omega}_v} \diagdown \right] \left[\diagdown \boldsymbol{G}_d^m \diagdown \right] \boldsymbol{\eta} \right), \quad (26)$$

where the matrices $\left[\diagdown \frac{\boldsymbol{\omega}_a}{\boldsymbol{s}+\boldsymbol{\omega}_a} \diagdown \right]$, $\left[\diagdown \frac{\boldsymbol{\omega}_s}{\boldsymbol{s}+\boldsymbol{\omega}_s} \diagdown \right]$ and $\left[\diagdown \frac{\boldsymbol{\omega}_v \boldsymbol{s}}{\boldsymbol{s}+\boldsymbol{\omega}_v} \diagdown \right]$ have now dimensions $(\overline{n}_m \times \overline{n}_m)$, while the modal controlled amplitudes are now redefined as functions of the true mirror displacement at controlled points, i.e. $\boldsymbol{\eta} = \boldsymbol{X}_c^{\dagger} \boldsymbol{d}$. An improved open loop plant transfer function can be obtained from Eqs. 21 and 26

$$\boldsymbol{\eta} = \left[\diagdown \frac{1}{\boldsymbol{s}^2 + 2\boldsymbol{\omega}_c \boldsymbol{\xi}_c + \boldsymbol{\omega}_c^2} \diagdown \right] \left[\diagdown \frac{\boldsymbol{\omega}_a}{\boldsymbol{s}+\boldsymbol{\omega}_a} \diagdown \right] \left[\diagdown \frac{\boldsymbol{\omega}_s}{\boldsymbol{s}+\boldsymbol{\omega}_s} \diagdown \right]$$
$$\left(\boldsymbol{u}_m^p + \left[\diagdown \frac{\boldsymbol{\omega}_v \boldsymbol{s}}{\boldsymbol{s}+\boldsymbol{\omega}_v} \diagdown \right] \boldsymbol{u}_m^d \right), \quad (27)$$

where $\boldsymbol{u}_m^p$ and $\boldsymbol{u}_m^d$ are respectively $(\overline{n}_m \times 1)$ vectors of proportional and derivative modal control forces. Eq. 27 highlights that the improved system description remains uncoupled if an IMSC philosophy is exploited.

Once the modal gain matrices $\left[\diagdown \boldsymbol{G}_p^m \diagdown \right]$ and $\left[\diagdown \boldsymbol{G}_d^m \diagdown \right]$ have been designed, for example through one of the two procedures presented in Sec. 3.6 and 3.7,

the corresponding gain matrices in physical space can be retrieved as

$$\boldsymbol{G}_p = \boldsymbol{X}_c^{T\dagger} \left[{}^{\searrow} \boldsymbol{G}_p^m {}_{\searrow} \right] \boldsymbol{X}_c^{\dagger}, \qquad \boldsymbol{G}_d = \boldsymbol{X}_c^{T\dagger} \left[{}^{\searrow} \boldsymbol{G}_d^m {}_{\searrow} \right] \boldsymbol{X}_c^{\dagger}. \qquad (28)$$

Thus the system FB contribution assumes the same structure as Eq. 15.

The gain matrices in physical space, Eq. 28, are fully populated. A distributed control cannot be obtained through an a priori decoupling of the plant model, as for the LQR and Mini-Max design. However, the gains coupling diminishes for increasing actuators distance. This suggests to neglect the coupling gains of actuators that are sufficiently distant from each other, see for example (Ruppel, 2012), in order to obtain a distributed control. Once again only the coupling terms of actuators belonging to the same control boards are retained. Of course, decoupling the system by dropping the smaller gain terms does not offer any mathematical guarantee on the final performances of the controller; this is especially true because the number of dropped terms is significant. However, as we shall see, the decoupled system performances appears to be acceptable.

3.6. Suboptimal stochastic IMSC design

The transfer function of Eq. 27, with the addition of possible system disturbances, can be realized in the time domain through $\overline{n}_m$ uncoupled state space systems, corresponding to each controlled modal shape,

$$\dot{\boldsymbol{x}}_{m_i} = \boldsymbol{A}_{m_i} \boldsymbol{x}_{m_i} + \boldsymbol{B}_m u_{m_i} + \boldsymbol{L}_m \boldsymbol{v}_{m_i},$$

$$\boldsymbol{y}_{m_i} = \boldsymbol{C}_m \boldsymbol{x}_{m_i}, \qquad (29)$$

with i ranging from 1 to $\overline{n}_m$. The (5×1) state space vector $\boldsymbol{x}_{m_i}$ corresponds to $\boldsymbol{x}_{m_i}^T = \left[\eta_i \ \dot{\eta}_i \ \eta_{s_i} \ u_{m_i}^a \ v_{\eta s_i} \right]$, where η_i and $\dot{\eta}_i$ are respectively the ith modal amplitude and velocity, η_{s_i} is the ith measured modal amplitude, $v_{\eta s_i}$ is the ith modal velocity obtained through the pseudo-derivative filter applied to

23

the measured modal amplitude, $u_{m_i}^a$ is the ith IMSC control force filtered by the actuator dynamics. A possible realization of the ith modal state space set of equations is

$$\boldsymbol{A}_{m_i} = \begin{bmatrix} 0 & 1 & 0 & 0 & 0 \\ -\omega_{c_i}^2 & -2\xi_{c_i}\omega_{c_i} & 0 & 1 & 0 \\ \omega_s & 0 & -\omega_s & 0 & 0 \\ 0 & 0 & 0 & -\omega_f & 0 \\ \omega_v\omega_s & 0 & -\omega_v\omega_s & 0 & -\omega_v \end{bmatrix},$$

$$\boldsymbol{B}_m = \begin{bmatrix} 0 \\ 0 \\ 0 \\ \omega_f \\ 0 \end{bmatrix}, \quad \boldsymbol{L}_m = \begin{bmatrix} 0 & 0 & 0 \\ 1 & 0 & 0 \\ 0 & \omega_s & 0 \\ 0 & 0 & \omega_f \\ 0 & 0 & 0 \end{bmatrix},$$

$$\boldsymbol{C}_m = \begin{bmatrix} 0 & 0 & 1 & 0 & 0 \\ 0 & 0 & 0 & 0 & 1 \end{bmatrix}, \tag{30}$$

where the (3×1) i^{th} modal disturbance vector, $\boldsymbol{v}_{m_i}^T = \begin{bmatrix} v_{m_i}^e & v_{m_i}^s & v_{m_i}^a \end{bmatrix}$, comprises an external disturbance $v_{m_i}^e$ acting on the mirror, a measurement disturbance $v_{m_i}^s$ and a control force disturbance $v_{m_i}^a$. With reference to Eq. 29 a direct output feedback $u_{m_i} = \boldsymbol{G}^{m_i}\boldsymbol{C}_m\boldsymbol{x}_{m_i} = [G_p^{m_i} \ G_d^{m_i}]\boldsymbol{C}_m\boldsymbol{x}_{m_i}$ can be envisioned (Kwakernaak and Sivan, 1972), where $G_p^{m_i}$ and $G_d^{m_i}$ are respectively the ith diagonal element of the modal gain matrices $\begin{bmatrix} \diagdown \boldsymbol{G}_p^m \diagdown \end{bmatrix}$ and $\begin{bmatrix} \diagdown \boldsymbol{G}_d^m \diagdown \end{bmatrix}$. This solution is clearly suboptimal if compared with an LQR stochastic full state control; it is thus dubbed a suboptimal stochastic design. This solution assumes the presence of stochastic disturbances, i.e. $\boldsymbol{v}_{m_i}$ needs to be ergodic noises with zero mean and (3×3) intensity matrix $\boldsymbol{W}_v$. The gain matrix $\boldsymbol{G}^{m_i}$ can be designed through the minimization of the functional

24

$J = \frac{1}{2} \mathrm{E} \left(\boldsymbol{x}_{m_i}^T \boldsymbol{Q} \boldsymbol{x}_{m_i} + u_{m_i} R u_{m_i} \right)$, i.e.

$$\min_{\boldsymbol{G}^{m_i}} (J), \tag{31}$$

where E() is the expectation operator, while $\boldsymbol{Q}$ and R are respectively the symmetric semipositive definite (5×5) state weight matrix and the scalar positive definite control force weight. The functional J of Eq. 31 can be rewritten, by resorting to the properties of the matrix trace operator, tr(), as

$$J = \frac{1}{2} \mathrm{tr} \left(\left(\boldsymbol{Q} + \boldsymbol{C}_m^T \boldsymbol{G}^{m_i T} R \boldsymbol{G}^{m_i} \boldsymbol{C}_m \right) \boldsymbol{\sigma}_{xx}^2 \right), \tag{32}$$

where the (5×5) state variance matrix $\boldsymbol{\sigma}_{xx}^2$ is solution of the Lyapunov equation

$$\overline{\boldsymbol{A}}_{m_i} \boldsymbol{\sigma}_{xx}^2 + \boldsymbol{\sigma}_{xx}^2 \overline{\boldsymbol{A}}_{m_i}^T + \boldsymbol{L}_m \boldsymbol{W}_v \boldsymbol{L}_m^T = \boldsymbol{0} \tag{33}$$

with $\overline{\boldsymbol{A}}_{m_i} = \boldsymbol{A}_{m_i} - \boldsymbol{B}_m \boldsymbol{G}^{m_i} \boldsymbol{C}_m$. The fixed structure of the gain matrix does not allow to determine $\boldsymbol{G}^{m_i}$ through the resolution of an ARE as for the LQR design. So the solution is sought by performing a numerical optimization of the functional, Eq. 32, subject to the constraint of Eq. 33. An unconstrained minimization allows to find a solution of Eq. 33 only if the initial gain matrix leads to a stable system. This is not a problem for the case at hand because the plant has no unstable poles, so it suffices to start the optimization with null or very small gains. The optimization can proceed without the explicit imposition of the system stability constraint because a loss of stability would cause a deterioration of the cost functional. Contrarily to the unique solution provided by the stochastic LQR design, the suboptimal problem can converge towards different local minima if different intensity matrix $\boldsymbol{W}_v$ are chosen. As already remarked at the end of Section 3.3, the overall difficulties and the computational costs of finding acceptable local minima for large MIMO control problems prevent the possibility of easily applying the suboptimal

25

design strategy to the coupled physical state space system description of Eq. 11, and this is even truer if the model is improved by adding the sensors, actuators and pseudo-derivative filters dynamics.

Efficient optimizers require (Nocedal and Wright, 2006) not only the evaluation of the cost functional, but also of its (2×1) gradient vector computed with respect to the optimization parameters $\boldsymbol{G}^{m_i}$

$$\boldsymbol{\nabla} J = \frac{1}{2} \left[\mathrm{tr} \left(\boldsymbol{F} \frac{\partial \boldsymbol{\sigma}_{xx}^2}{\partial G_p^{m_i}} \right) \ \mathrm{tr} \left(\boldsymbol{F} \frac{\partial \boldsymbol{\sigma}_{xx}^2}{\partial G_d^{m_i}} \right) \right]^T. \tag{34}$$

The gradient vector can be efficiently computed as

$$\boldsymbol{\nabla} J = \left[\mathrm{tr} \left(\boldsymbol{\Lambda} \frac{\partial \overline{\boldsymbol{A}}_{m_i}}{\partial G_p^{m_i}} \boldsymbol{\sigma}_{xx} \right) \ \mathrm{tr} \left(\boldsymbol{\Lambda} \frac{\partial \overline{\boldsymbol{A}}_{m_i}}{\partial G_d^{m_i}} \boldsymbol{\sigma}_{xx} \right) \right]^T, \tag{35}$$

where the (5×5) Lagrange multipliers matrix $\boldsymbol{\Lambda}$ can be obtained through the resolution of the adjoint Lyapunov equation

$$\overline{\boldsymbol{A}}_{m_i} \boldsymbol{\Lambda} + \boldsymbol{\Lambda} \overline{\boldsymbol{A}}_{m_i}^T + \boldsymbol{F} = \boldsymbol{0}. \tag{36}$$

The cost functional gradient requires the solution of only one Lyapunov equation, Eq. 36, and the computation of the derivatives $\frac{\partial \overline{\boldsymbol{A}}_{m_i}}{\partial \boldsymbol{G}^{m_i}}$.

3.7. Closed loop poles optimization, IMSC design

A different approach is to optimize the pole locations of each uncoupled closed loop modal transfer function. Starting from Eq. 27, the ith modal open loop transfer function $L_{TF_i}(s)$ can be written as

$$L_{TF_i}^{ol} = \left[\diagdown \frac{1}{s^2 + 2\omega_{c_i} \xi_{c_i} + \omega_{c_i}^2} \diagdown \right] \left[\diagdown \frac{\omega_a}{s + \omega_a} \diagdown \right]$$
$$\left[\diagdown \frac{\omega_s}{s + \omega_s} \diagdown \right] \left(G_p^{m_i} + \left[\diagdown \frac{\omega_v s}{s + \omega_v} \diagdown \right] G_d^{m_i} \right), \tag{37}$$

so that the closed loop transfer function is

$$L_{TF_i}^{cl} = \frac{L_{TF_i}^{ol}}{L_{TF_i}^{ol} + 1}. \tag{38}$$

An exact closed loop pole placement for Eq. 38 is not feasible without the introduction of an observer of the complete state of the system. However, if the ith modal response is dominated by two complex conjugate poles, i.e. if the response can be approximated by a second order system, then a constrained optimization of the closed loop system poles allows to reasonably match the desired second order modal response.

The problem can be stated in mathematical terms as a constrained optimization procedure

$$
\begin{aligned}
&\min_{\boldsymbol{G}^{m_i}} (J) \text{ such that} \\
&\text{Re}\,(\boldsymbol{\lambda}_i) < 0, \\
&G_p^{m_i} \geq 0 \quad G_d^{m_i} \geq 0,
\end{aligned}
\tag{39}
$$

where $J = \min\left(|\boldsymbol{\lambda}_i - \overline{\lambda}_i|\right) + \min\left(|\boldsymbol{\lambda}_i - \overline{\lambda}_i^*|\right)$, $\boldsymbol{\lambda}_i$ is the (5×1) vector of the closed loop poles belonging to the ith modal contribution, the scalars $\overline{\lambda}_i$ and $\overline{\lambda}_i^*$ represent respectively the desired pole location for the ith modal contribution and its complex coniugate and $|\cdot|$ computes the absolute value of each vector component.

The suboptimal stochastic design requires the choice of appropriate weighting matrices and system disturbances, which are usually found through trial and errors procedures. The closed loop poles optimization, instead, requires choosing appropriate desired pole locations. Its remarkable advantage is that the poles location is easily linked with well known performance indexes of second order systems. In fact, the overshoot, O_{r_i}, and the settling time, T_{ε_i}, of the ith approximated modal second order system response to step input

can be expressed as

$$O_{r_i} = \exp\left(-\frac{\overline{\xi}_i \pi}{\sqrt{1 - \overline{\xi}_i^2}}\right),$$

$$T_{\varepsilon_i} \approx \frac{1}{\overline{\omega}_i \overline{\xi}_i} \ln\left(\frac{1}{\varepsilon \sqrt{1 - \overline{\xi}_i^2}}\right), \tag{40}$$

where $\overline{\xi}_i$ and $\overline{\omega}_i$ are respectively the desired second order system damping coefficient and circular frequency, while ε defines the settling time as the time required to set the response within the region $\pm\varepsilon$ the final steady value. So the designer can choose the desired response overshoot and settling time for each controlled modal contribution, i.e. set the parameters O_{r_i}, T_{ε_i} and ε. Than, by solving the first uncoupled non linear Eqs. 40, $\overline{\xi}_i$ can be determined and introduced in the second of Eqs. 40 that can be solved for $\overline{\omega}_i$. Finally, the desired poles for the ith modal response are

$$\left\{\overline{\lambda}_i, \overline{\lambda}_i^*\right\} = -\overline{\xi}_i \overline{\omega}_i \pm i\,\overline{\omega}_i \sqrt{1 - \overline{\xi}_i^2}. \tag{41}$$

Of course the constrained optimization procedure does not guarantee an exact pole placement. Moreover, the nominal plant response may differ from a pure second order one, especially when the ith modal circular frequency is close to the sensors, actuators or pseudo-derivative filter own dynamics. However the frequency separation is always sufficiently large for the case at hand. Thus, the second order approximation is a viable approach to the control system design. Although the sought overshoot and settling time could be different for every nominal plant vibration mode, we have limited our investigation to controllers designed by imposing the same values to every mode. This is inline with the usual specifications provided in terms of modal responses of deformable mirrors in adaptive optics.

28

4. Nominal plant and robust stability criterium

The control design procedures introduced in the previous sections are based on a nominal plant description. The mass, damping and stiffness matrices condensed at the actuation points of Eq. 14 could be assumed to be the same as those required by the static and dynamic FF of Eqs. 8 and 7. These matrices can be tuned (Manetti et al., 2010) or identified (Manetti, 2011) directly in the field. The matrices $\boldsymbol{M}$, $\boldsymbol{C}$ and $\boldsymbol{K}$ are symmetric positive definite, but the identified matrices $\boldsymbol{M}^*$, $\boldsymbol{C}^*$ and $\boldsymbol{K}^*$ are not, mainly because of the inexact sensors co-location (Manetti et al., 2012b). The ideal condensed matrices can be computed from the mirror FE model exploited to simulate the system (see Sec. 2 and references therein); however the damping contribution is dominated by fluid dynamics, while the FE model structural description is undamped. In the following the stiffness matrix $\boldsymbol{K}$ is computed from the FE model of the mirror. The mass and damping matrices, instead, are assumed to be diagonal. The lumped mass matrix $\boldsymbol{M}$ will have all the diagonal terms equal to the system mass divided by the number of actuation points, as suggested in (Manetti et al., 2010) for $\boldsymbol{M}^*$. The damping matrix $\boldsymbol{C}$ is derived from the identified matrix $\boldsymbol{C}^*$, which has been verified to have a strong diagonal dominance in (Manetti, 2011). These modeling choices lead to an adequately accurate description of the system static response. The plant dynamics, instead, are approximated to well match the actual plant response for frequencies up to about 4200 Hz, a sufficiently high frequency for the required control system bandwidth.

As anticipated in Sec. 3.5, the modal plant description, Eq. 21, exploits part of the modal analysis performed on the accurate FE model, i.e. the controlled modal circular frequencies $\boldsymbol{\omega_c}$ and the controlled modal shapes $\boldsymbol{X}_c$ are the first $\overline{n}_m$ controllable and observable modal contributions of Eq. 1.

Once again, the modal damping coefficients $\boldsymbol{\xi}_c$ have to adequately describe both the structural and fluid dynamic damping. They can be estimated from the physical coordinates plant model of Eq. 11, built using the approximated mass, damping and stiffness matrices of the previous paragraph: carring out an eigenvalue analysis the first $\overline{n}_m$ couples of complex conjugate eigenvalues allow to estimate the corresponding damping coefficients associated to the controlled modal shapes.

All the control design procedures shown in the previous sections have very good stabilizing properties with respect to the nominal plant. However differences between the nominal and real system may reduce system stability, a critical point for large deformable mirrors. This is mainly related to control spillover on the frequencies beyond those well described by the nominal plant. The high modal density of deformable mirrors prevents the introduction of a sufficiently sharp control action attenuation beyond the control bandwidth without adding a sizable destabilizing phase lag. Fluid dynamics damping is quite large in the low frequency range, but diminishes at higher frequencies, where the phase lags of sensors, actuators and pseudo-derivative filters becomes appreciable as well. The development of a nominal plant model that is accurate over a larger frequency range would be a daunting task because of the problem size and of the difficulty of describing, even with the accurate simulator of Sec. 2, the high frequency system damping. These reasons suggest to analyze the stability robustness with respect to high frequency plant uncertainty for all of the control system designs introduced in previous sections, so to warrant the stability of the real plant.

The related stability robustness measure can also be exploited to compare the different controllers. Therefore, their gains will be tuned in order to grant the same degree of stability robustness, thus allowing a fair comparison of
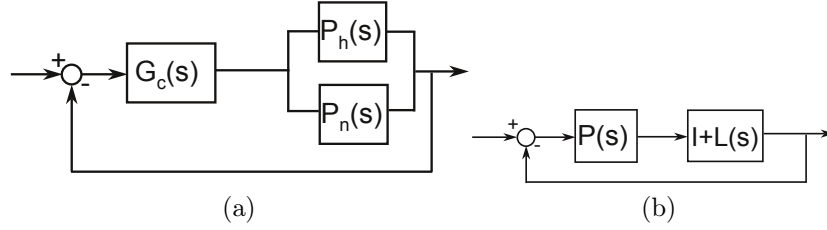
Figure 6: Block diagram description to study control system stability robustness.

the different solutions.

The block diagram of Fig. 6a represents a generic nominal plant transfer matrix $\boldsymbol{P}_n$ with an additive high frequency uncertainty $\boldsymbol{P}_h$ and a feedback controller $\boldsymbol{G}_c$.

The additive uncertainty of Fig. 6a can be transformed into the multiplicative uncertainty at the plant output of Fig. 6b by simply defining the transfer matrices $\boldsymbol{P} = \boldsymbol{P}_n \boldsymbol{G}_c$ and $\boldsymbol{L} = \boldsymbol{P}_h \boldsymbol{P}_n^{-1}$ (e.g. Bastaits et al., 2009). If the controller verifies the nominal plant stability, then the stability of the system perturbed through the uncertainty $\boldsymbol{P}_h$ placed at the plant output is guaranteed when (Doyle and Stein, 1981)

$$\overline{\sigma}\left(\boldsymbol{P}(j\omega)\left(\boldsymbol{I} + \boldsymbol{P}(j\omega)\right)^{-1}\right) < 1/\overline{\sigma}\left(\boldsymbol{L}(j\omega)\right) \qquad \forall \omega > 0. \qquad (42)$$

As already explained, the stability robustness level is here exploited as a mean to compare the performances of different control designs. Thus, to grant a meaningful comparison, the very same nominal plant has to be used for all the controllers. The nominal modal system description has been used for such a check over all the proposed solutions, verifying the nominal stability of all the control designs by comparing the eigenvalues of the system state space realization.

For the case at hand the high frequency uncertainty is modeled as a

Parameters	Values
$\overline{n}_m$	150
n_m^h	4850
ω_h^{min}	870·2π (rad/sec)
ω_h^{max}	32400·2π (rad/sec)
$\xi_h(\omega_h^{min})$	0.05
$\xi_h(\omega_h^{max})$	0.0001
ω_a	25000·2π (rad/sec)
ω_s	25000·2π (rad/sec)
ω_v	15000·2π (rad/sec)

Table 1: System parameters.

$(n_a \times n_a)$ transfer matrix

$$\boldsymbol{P}_h = \boldsymbol{X}_h \left[\searrow \frac{1}{s^2 + 2\xi_h \omega_h s + \omega_h^2} \searrow \right] \boldsymbol{X}_h^T, \qquad (43)$$

with $\boldsymbol{X}_h$ a $(n_a \times n_m^h)$ matrix containing the n_m^h high frequency modal shapes not appropriately described by $\boldsymbol{P}_n$; ω_h and ξ_h are respectively the high frequency circular frequencies and damping coefficients. The high frequency fluid dynamics contribution is accounted for by tuning the damping coefficient ξ_h, which is here conservatively approximated as linearly varying between the lower and the higher residual modal frequencies, ω_h^{min} and ω_h^{max}. The number of controlled modes $\overline{n}_m$ is kept smaller than the number of actuators, $\overline{n}_m < n_a$, as explained in Section 3.5. The lower uncontrolled modes frequency, ω_h^{min}, is determined by $\overline{n}_m$. The number n_m^h of high frequency modal shapes not appropriately described by $\boldsymbol{P}_n$ covers a wide frequency range, up to ω_h^{max}, so to guarantee the absence of spillover. The sensors, actuators and pseudo-derivative filters frequencies ω_s, ω_a and ω_v are typical of current implementations. The high frequency modal parameters are resumed in Table 1.

(a) Centralized control designs   (b) IMSC, suboptimal stochastic design and PD
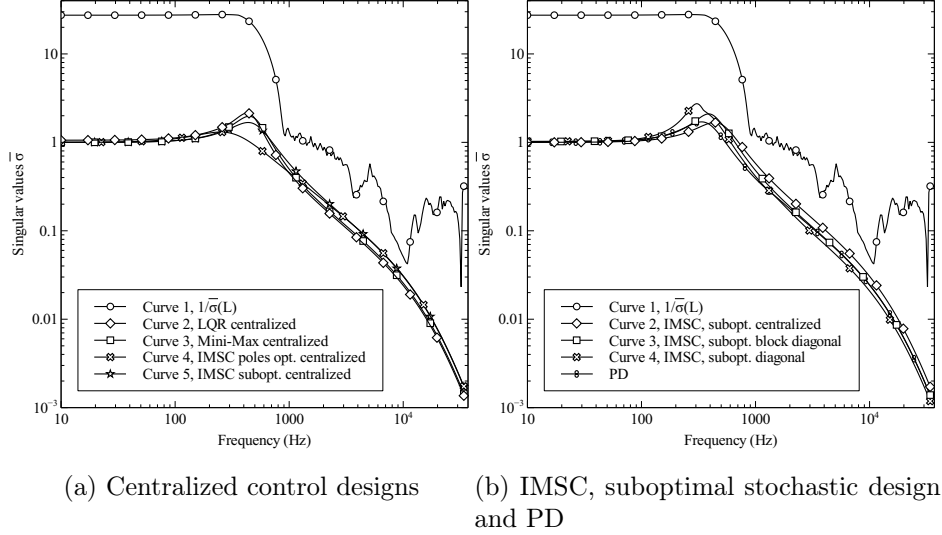
Figure 7: Stability robustness verification of different control design schemes.

5. Simulation results

The design weights and performance parameters of each of the controllers of Sec. 3 are first tweaked in order to obtain comparable system stability robustness. Figure 7a shows the satisfaction of the robust stability condition for all the four completely centralized control design techniques. Curve 1 represents the right-hand term of Eq. 42, and is equal for all the controllers. The other curves are the left-hand term and guarantee almost the same stability robustness degree. The different implementations of the IMSC suboptimal stochastic design are compared in Fig. 7b along with the completely decentralized FB with constant proportional and derivative diagonal gain matrices (PD). The IMSC suboptimal diagonal curve of Figure 7b is for a completely decentralized control system. The decentralized control has been obtained by following the block diagonal design procedure, while reducing the block size to a single actuator.

The different designs have been tested through the simulation of the GMT

(nm)	PD	LQR	Mini Max	IMSC, poles opt.	IMSC, subopt.
Centralized	–	4.8	4.5	5.7	4.7
Block diagonal	–	5.2	4.5	5.4	4.8
Diagonal	4.8	5.0	4.6	4.7	5.0
Centralized turb.	–	9.4	9.5	13.9	7.9
Block diagonal turb.	–	18.7	9.8	16.9	10.4
Diagonal turb.	22.1	21.2	12.3	14.5	20.7

Table 2: rms tracking error of different control designs, without and with (turb.) wind turbulence .

on-axis secondary adaptive mirror. The mirror must track a realistic command history of 0.3 s, with a step command rate of 2 kHz. The chosen time history represents a bad seeing conditions, i.e. a 90th percentile seeing, and has been provided by the GMT working group. All the analyses have been performed with and without wind turbulence. Table 2 summarizes the rms tracking error computed over all the actuation points at each control step and then throughout the simulation. It should be noticed that the reported results are obtained by assuming that the computational delay required to evaluate the FB actions is the same for all the control schemes, and close to the computational delay required by the current hardware to evaluate the PD FB term. Such an assumption implies an adequate parallelization of the control hardware. All the control techniques and gain matrices topologies appears to have comparable rms tracking errors when the wind disturbance is not accounted for in the simulation. In fact, without wind turbulence the performances are mainly limited by the technology at hand. On the contrary the system capabilities in presence impinging turbulence, do depend on the different control strategies and implementations. As expected, the best performances are achieved by exploiting a fully centralized gain structure; the completely decentralized solutions show the worst performances,

and the partially centralized ones are in between. The only exception to this trend is the IMSC with poles optimization, whose diagonal implementation provides slightly better results than those of its distributed solution. The mere fact that the fully centralized solutions have better performances than decentralized ones is by no means surprising. Less granted, due to the topological limitations imposed by the technology, are the results of block diagonal implementations. It is interesting to discuss the actual amount of performance losses in relation to the adopted control design techniques. The LQR centralized design halves the rms tracking error of the diagonal implementation, while the performances of its block-diagonal implementation are closer to those of the diagonal solution. The IMSC suboptimal results are comparable to those of the LQR controller, but its block diagonal implementation is more efficient, with an rms error closer to that of the centralized solution. The Mini-Max control proves to have a remarkably small dependence on the controller topology. Its centralized and block-diagonal versions are almost equivalent, and the diagonal implementation is not much worse. The Mini-Max design for large values of the parameter γ (see Eq. 17) leads to a solution that is equivalent to the LQR design. However, as shown in the Appendix, lower γ values move the gain matrices topology toward a diagonal structure, which is at the core of a better controller robustness. This is confirmed by the fact that it is necessary to increase the gain matrices of all the diagonal implementations in order to obtain the same degree of stability robustness of the distributed controllers. However the Mini-Max design provides an intrinsic diagonal dominance of the gain matrices structure, leading to a low performance sensitivity with respect to topology variations.

Fig. 8a shows the rms tracking error frequency spectrum obtained using the IMSC suboptimal stochastic design, computed at all of the actuation

35

(a) IMSC suboptimal design.

(b) Mini-Max design.
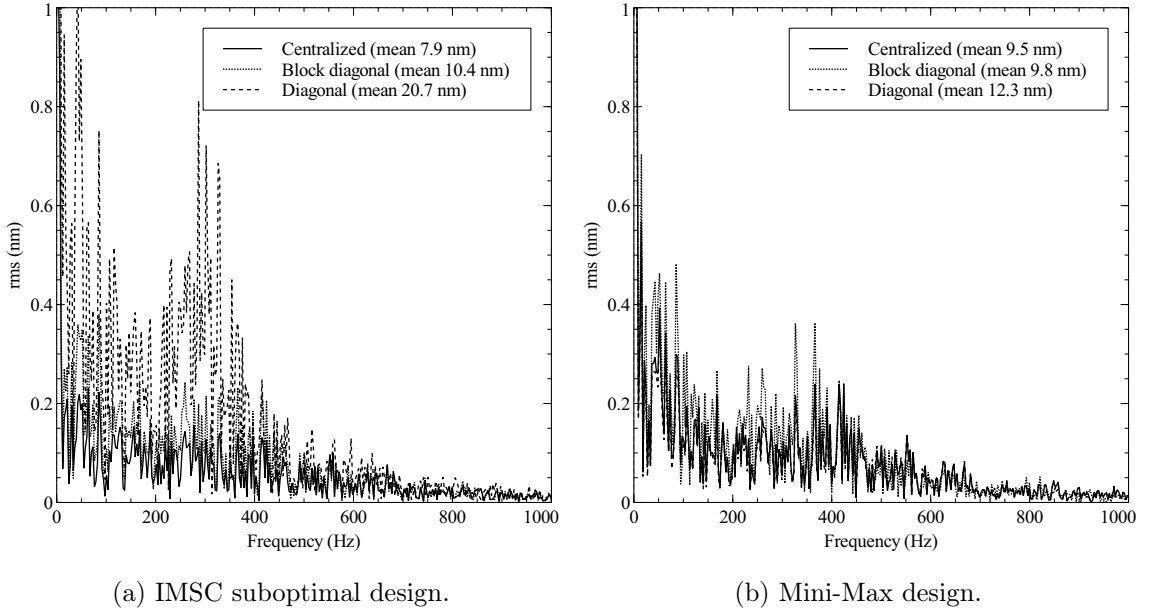
Figure 8: Rms tracking error frequency spectrum.

points at each control step. The rms error decreases slowly with frequency and goes to almost zero above 1000 Hz. The performance improvements granted by the centralized and distributed control solutions should be quite clear. The other control schemes, such as the Mini-Max design of Figure 8b, are characterized by similar trends. The corresponding position time histories for a representative actuator are shown in Fig. 9, and confirm the improvement in tracking that is achievable with full or partial feedback centralization.

Table 3 compares the results obtained with a different set of controllers. The constant diagonal gain result is obtained by using a completely decentralized FB with constant proportional and derivative diagonal gain matrices, much like that implemented in operational mirrors[1]. The rms tracking error

---

[1]Operational mirrors actually have different gains between external and internal actuator rings to better account for different stiffnesses and air damping at their boundaries.
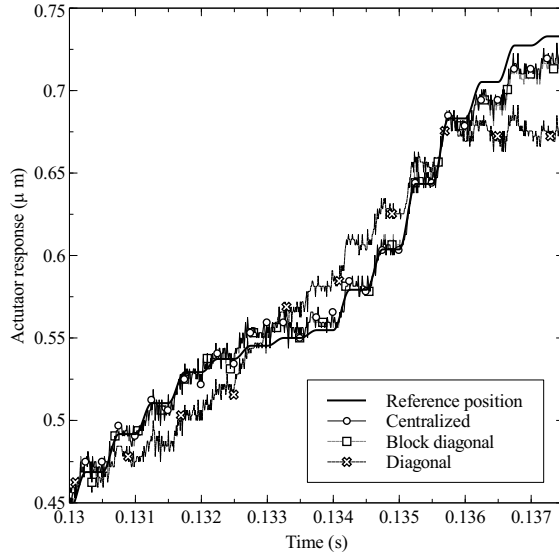
Figure 9: Tracking performances in presence of wind disturbances of the IMSC suboptimal design implemented as: centralized, distributed and diagonal.

Control techniques	rms (nm)
Constant diagonal gain matrices (PD)	22.1
IMSC suboptimal, distance–based band topology	8.6
IMSC suboptimal, block diagonal	10.4
IMSC suboptimal, diagonal	20.7
IMSC suboptimal centralized without FF terms	827

Table 3: rms tracking error of different control designs, in presence of wind turbulence disturbances.

of 22.1 nm confirms the validity of this choice, even if through an appropriate gains design the very same completely decentralized scheme could be improved, as shown in Table 2. The IMSC suboptimal distance–based band topology rms is obtained with a more traditional distributed strategy, where each actuation point is coupled with all the actuators within 0.1 m, with an overall number of coupled actuators comparable to that of each square sectors in Fig. 4. The resulting rms error of 8.6 nm is placed between the completely centralized solution (7.9 nm) and the block diagonal one (10.4 nm). This

result confirms that the block diagonal topology performances are negatively affected by the need to neglect the coupling with all the nearby actuators that are assigned to different control boards. However, it also highlights the fact that the resulting performance loss is not substantial. Hence, it justifies the proposed approach. Moreover, the possibility of using the current hardware without the need of any data exchange between different control board well compensates the inevitable slight performance loss that has to be payed. It is remarked that the last line of Table 3 well emphasizes that no useful results can be obtained without the any FF.

6. Concluding remarks

This paper evaluates possible FB control improvements for large deformable mirrors applied to adaptive optics. The work compares four different control techniques, each implemented with a completely centralized, partially centralized and completely decentralized structure.

The controllers performance are compared after tuning their gains so to assure almost the same stability robustness with respect to high frequency modal uncertainties.

The analysis highlights significant differences in performance only when the mirror is affected by directly impinging external wind turbulence. As expected the best results are achieved by completely centralized solutions, with partially centralized controllers providing better results than completely decentralized ones.

The IMSC suboptimal centralized and block-diagonal stochastic design assures very good performances in face of wind disturbances. The Mini-Max control provides the best partially centralized and completely decentralized solutions. This controller shows that a strong diagonal dominance of the gain matrices improves the design stability robustness, albeit at the expense of

38

slight performance decrements, so posing itself as a suitable design techinque for completely decentralized solutions.

All the completely decentralized solutions provide results that are better than those of a more traditional PD control with equal gains at all the actuation points. The simulated results confirm also that the performance loss incurred by decoupling nearby actuators belonging to different control boards is limited to 31%, at most, for all but the LQR controller.

The leading role of the FF contributions is confirmed once more. In fact, it has been verified that even the best fully centralized design is not able to assure satisfactory performances without the presence of an appropriate FF. This is because the system stability constraint prevents the use of sufficiently high FB gains and thus the possibility of an accurate command tracking.

Appendix

This appendix justifies the assertion that for a small γ and a diagonal plant mass matrix M (cfr. Section 4) the gain matrix of the Mini-Max controller tends, for the case at hand, towards a diagonal structure. By partitioning the matrices P and Q as

$$P = \begin{bmatrix} P_{dd} & P_{\dot{d}d}^T \\ P_{\dot{d}d} & P_{\dot{d}\dot{d}} \end{bmatrix} \qquad Q = \begin{bmatrix} Q_{dd} & 0 \\ 0 & Q_{\dot{d}\dot{d}} \end{bmatrix} \qquad (44)$$

and recalling the definition of the matrix B of Eq. 14, the gain matrix turns out to be:

$$G = R^{-1}M^{-1} \begin{bmatrix} P_{\dot{d}d} & P_{\dot{d}\dot{d}} \end{bmatrix} = [G_p G_d]. \qquad (45)$$

Recalling that we have assumed $L = B$ and diagonal R and Q, Eq. 18 makes it clear that G would be diagonal whenever $P_{\dot{d}d}$ and $P_{\dot{d}\dot{d}}$ are so. Partitioning

39

the ARE Eq. 20 according to Eq. 44 one obtains:

$$-\boldsymbol{P}_{\dot{d}d}^{T}\boldsymbol{M}^{-1}\boldsymbol{K} - \left(\boldsymbol{P}_{\dot{d}d}^{T}\boldsymbol{M}^{-1}\boldsymbol{K}\right)^{T} - \boldsymbol{P}_{\dot{d}d}^{T}\boldsymbol{V}\boldsymbol{P}_{\dot{d}d} + \boldsymbol{Q}_{dd} = \boldsymbol{0}, \quad (46)$$

$$\boldsymbol{P}_{\dot{d}d}^{T} + \boldsymbol{P}_{\dot{d}d} - \boldsymbol{P}_{\dot{d}\dot{d}}\boldsymbol{M}^{-1}\boldsymbol{C} - \left(\boldsymbol{P}_{\dot{d}\dot{d}}\boldsymbol{M}^{-1}\boldsymbol{C}\right)^{T} + \boldsymbol{P}_{\dot{d}\dot{d}}\boldsymbol{V}\boldsymbol{P}_{\dot{d}\dot{d}} + \boldsymbol{Q}_{\dot{d}\dot{d}} = \boldsymbol{0}, \quad (47)$$

with $\boldsymbol{V} = \boldsymbol{M}^{-1}\left(\boldsymbol{R}^{-1} - \frac{1}{\gamma^2}\boldsymbol{I}\right)\boldsymbol{M}^{-T}$, where a third equation, needed to evaluate $\boldsymbol{P}_{dd}$ after $\boldsymbol{P}_{\dot{d}d}$ and $\boldsymbol{P}_{\dot{d}\dot{d}}$, has been omitted, since it is of no interest for $\boldsymbol{G}$. Consider at first Eq. 46 and rewrite it as:

$$-\boldsymbol{P}_{\dot{d}d}^{T}\boldsymbol{E} - \boldsymbol{E}^{T}\boldsymbol{P}_{\dot{d}d} - \boldsymbol{P}_{\dot{d}d}^{T}\boldsymbol{M}^{-1}\boldsymbol{F}\boldsymbol{M}^{-T}\boldsymbol{P}_{\dot{d}d} + \boldsymbol{Q}_{dd} = \boldsymbol{0}, \qquad (48)$$

with $\boldsymbol{E} = \boldsymbol{M}^{-1}\boldsymbol{K} + \gamma^{-2}\boldsymbol{M}^{-1}\boldsymbol{M}^{-T}\boldsymbol{P}_{dd}$ and $\boldsymbol{F} = \boldsymbol{R}^{-1} + \gamma^{-2}\boldsymbol{I}$. Now, conjecturing that $\boldsymbol{P}_{\dot{d}d}$ scales as γ, it is possible to see that the terms $\boldsymbol{M}^{-1}\boldsymbol{K}$ of $\boldsymbol{E}$ and $\boldsymbol{R}^{-1}$ of $\boldsymbol{F}$ become negligible as $\gamma \to 0$, so that the only significant terms of Eq. 46 would be $-\frac{1}{\gamma^2}\boldsymbol{P}_{\dot{d}d}\boldsymbol{M}^{-1}\boldsymbol{M}^{-T}\boldsymbol{P}_{\dot{d}d}^{T} + \boldsymbol{Q}_{dd} = \boldsymbol{0}$. Being $\boldsymbol{M}$ the scalar matrix of the uniformly lumped mirror mass m we have: $\boldsymbol{P}_{\dot{d}d} = \gamma m \sqrt{\boldsymbol{Q}_{dd}}$ if $\boldsymbol{Q}_{dd}$ is diagonal, as it indeed is for our case. A similar result, i.e. $\boldsymbol{P}_{\dot{d}\dot{d}} = \gamma m \sqrt{\boldsymbol{Q}_{\dot{d}\dot{d}} + 2\boldsymbol{P}_{\dot{d}d}}$, will be obtained by applying the very same reasoning to Eq. 47, thus confirming the assumed proportionality of $\boldsymbol{P}$ with respect to γ. Similar steps, albeit for a slightly different problem, can be found in Friedland (1986).

As said in Section 3.4, there is an inferior limit γ_{min} allowed. So the above result would be more or less satisfied in relation to the value γ_{min} usable for the application at hand. A substantial diagonalization has been verified to actually occur in our case. It is furthermore remarked that inserting the gain matrix of Eq. 45 into Eq. 13 leads to the following closed loop model in physical coordinates

$$\boldsymbol{M}\ddot{\boldsymbol{p}} + (\boldsymbol{C} + \boldsymbol{R}^{-1}\boldsymbol{M}^{-1}\boldsymbol{P}_{\dot{d}\dot{d}})\dot{\boldsymbol{p}} + (\boldsymbol{K} + \boldsymbol{R}^{-1}\boldsymbol{M}^{-1}\boldsymbol{P}_{\dot{d}d})\boldsymbol{p} = \boldsymbol{0}. \qquad (49)$$

So that, being $\boldsymbol{P}_{\dot{d}d}$ and $\boldsymbol{P}_{\dot{d}\dot{d}}$ as positive defined as the related $\boldsymbol{Q}_{dd}$ and $\boldsymbol{Q}_{\dot{d}\dot{d}}$ terms, the active controller ideally adds a true damping and stiffness to the system.

Without entering in further details we remark that for $\gamma = \infty$ and scalar matrices $\boldsymbol{R}$ and $\boldsymbol{M}$ the solution of Eqs. 46 and 47 will provide at least symmetric positive semidefinite $\boldsymbol{P}_{\dot{d}d}$ and $\boldsymbol{P}_{\dot{d}\dot{d}}$, once more depending on the $\boldsymbol{Q}_{dd}$ and $\boldsymbol{Q}_{\dot{d}\dot{d}}$ terms (Hanks and Skelton, 1991). Therefore what just said about the addition of an active damping and stiffness applies to the LQR controller as well. It is remarked that the design parameters used in this paper are only approximatively related to those defined in (Hanks and Skelton, 1991). Nevertheless, they are adequate enough to provide $\boldsymbol{P}_{\dot{d}d}$ and $\boldsymbol{P}_{\dot{d}\dot{d}}$ reasonably approximating symmetry and positive definiteness. Then, due to the at least semipositive definite active damping and stiffness blocks they provide by our optimal decentralized design with reduced order models, no stability issue will result when they are applied to the whole nominal mirror model. Therefore, once the same robustness stability bound has been reached, there remain just the problem of tuning the design weight for maximum performances.

Bibliography

Bastaits R, Rodrigues G, Mokrani B and Preumont A (2009) Active optics of large segmented mirrors: Dynamics and control. *Journal of Guidance, Control, and Dynamics* 32(6): 1795–1803, ISSN 0731-5090, DOI: 10.2514/1.44041.

Biasi R, Andrighettoni M, Angerer G, Mair C, Pescoller D, Lazzarini P, Anaclerio E, Mantegazza M, Gallieni D, Vernet E, Arsenault R, Madec PY, Duhoux P, Riccardi A, Xompero M, Briguglio R, Manetti M and Morandini M (2012) VLT deformable secondary mirror: integration and electromechanical tests results. In: Ellerbroek BL, Marchetti E and Véran JP (eds) *Adaptive Optics Systems III*, SPIE, vol. 8447, pp. 84472G–84472G, DOI: 10.1117/12.927087.

Biasi R and Gallieni D (2011) Contactless large deformable mirrors: ELT AO corrector technology available now. In: *Second International Conference on Adaptive Optics for Extremely Large Telescopes*, Victoria (BC), Canada, URL http://ao4elt2.lesia.obspm.fr/spip.php?article709.

Biasi R, Veronese D, Andrighettoni M, Angerer G, Gallieni D, Mantegazza M, Tintori M, Lazzarini PG, Manetti M, Johns M, Hinz P and Kern J (2010) GMT adaptive secondary design. In: Ellerbroek BL, Hart M, Hubin N and Wizinowich P (eds) *Adaptive Optics Systems II*, San Diego, California, USA: SPIE, vol. 7736, pp. 77363O–77363O–10, DOI: 10.1117/12.857983.

Bouchez AH, Acton DS, Agapito G, Arcidiacono C, Bennet F, Biliotti V, Bonaglia M, Briguglio R, Brusa-Zappellini G, Busoni L, Carbonaro L, Codona JL, Conan R, Connors T, Durney O, Espeland B, Esposito S, Fini L, Gardhouse R, Gauron TM, Hart M, Hinz PM, Kanneganti S, Kib-

blewhite EJ, Knox RP, McLeod BA, McMahon T, Montoya M, Norton TJ, Ordway MP, d'Orgeville C, Parcell S, Piatrou PK, Pinna E, Price I, Puglisi A, Quiros-Pacheco F, Riccardi A, Roll JB, Trancho G, Uhlendorf K, Vaitheeswaran V, van Dam MA, Weaver D and Xompero M (2012) The Giant Magellan Telescope adaptive optics program. In: *Adaptive Optics Systems III*, Amsterdam: SPIE, vol. 8447, pp. 84471I–84471I–12, DOI: 10.1117/12.926691.

Brusa-Zappellini G, Riccardi A, Ragland S, Esposito S, Del Vecchio C, Fini L, Stefanini P, Biliotti V, Ranfagni P, Salinari P, Gallieni D, Biasi R, Mantegazza P, Sciocco G, Noviello G and Invernizzi S (1998) Adaptive secondary P30 prototype: Laboratory results. In: *Proceedings SPIE, Adaptive Optical System Technologies*, Kona, Hawaii, vol. 3353, pp. 764–775, DOI: 10.1117/12.321693.

Colaneri P, Geromel JC and Locatelli A (1997) *Control Theory and Design: An RH2 and RH Viewpoint.* Academic Press, ISBN 9780080503103.

Davies R and Kasper M (2012) Adaptive optics for astronomy. *Annual Review of Astronomy and Astrophysics* 50: 305–351, DOI: 10.1146/annurev-astro-081811-125447.

Doyle J and Stein G (1981) Multivariable feedback design: Concepts for a classical/modern synthesis. *IEEE Transactions on Automatic Control* 26(1): 4– 16, ISSN 0018-9286, DOI: 10.1109/TAC.1981.1102555.

Ellenbroek R, Verhaegen M, Doelman N, Hamelinck R, Rosielle N, Steinbuch M, Ellerbroek BL and Calia DB (2006) Distributed control in adaptive optics: Deformable mirror and turbulence modeling. In: *Advances in Adap-*

tive Optics II, Orlando, FL, USA: SPIE, vol. 6272, pp. 62723K–62723K–12, DOI: 10.1117/12.671688.

Ercoli Finzi A, Lanz M and Mantegazza P (1985) Active structural control with decentralized and colocated control units. In: Meirovitch L (ed) *Dynamics and Control of Large Structures, proceedings of the Fifth VPI&SU/AIAA Symposium*, Blacksburg, Virginia, pp. 487–501.

Friedland B (1986) *Control system design: an introduction to state-space methods*. McGraw-Hill, ISBN 9780070224414.

Gallieni D, Tintori M, Mantegazza M, Anaclerio E, Crimella L, Acerboni M, Biasi R, Angerer G, Andrigettoni M, Merler A, Veronese D, Carel J, Marque G, Molinari E, Tresoldi D, Toso G, Spano P, Riva M, Mazzoleni R, Riccardi A, Mantegazza P, Manetti M, Morandini M, Vernet E, Hubin N, Jochum L, Madec P, Dimmler M and Koch F (2009) Voice-coil technology for the E-ELT m4 adaptive unit. In: *International Conference on Adaptive Optics for Extremely Large Telescopes*, Paris, France, DOI: 10.1051/ao4elt/201006002.

Gawronsky W (2004) *Advanced Structural Dynamics and Active Control of Structures*. Springer, ISBN 978-0-387-72133-0.

Géradin M and Rixen D (1997) *Mechanical vibrations: theory and application to structural dynamics*. John Wiley, ISBN 9780471975243.

Grocott SCO (1997) *Dynamic reconstruction and multivariable control for force-actuated, thin facesheet adaptive optics*. Ph.D. thesis, MIT, URL `http://adsabs.harvard.edu/abs/1997PhDT........89G`.

Grocott SCO and Miller DW (1997) Robust control of the mmt adaptive

secondary mirror. In: *Proc. SPIE Adaptive Optics and Applications*, vol. 3126, pp. 405–416, DOI: 10.1117/12.279052.

Hanks BR and Skelton RE (1991) *Closed-form solutions for linear regulator design of mechanical systems including optimal weighting matrix selection.* Tech. Rep. NASA Technical Memorandum 104052, NASA, March 1991, URL http://ntrs.nasa.gov/search.jsp?R=19910012259.

Hardy J (1998) *Adaptive Optics for Astronomical Telescopes.* New York: Oxford University Press, ISBN 978-0-19-509019-2.

Heimsten R, MacMynowski DG, Andersen T and Owner-Petersen M (2012a) Concept, modeling, and performance prediction of a low-cost, large deformable mirror. *Applied Optics* 51(5): 515, ISSN 0003-6935, 1539-4522, DOI: 10.1364/AO.51.000515.

Heimsten R, Owner-Petersen M, Ruppel T, MacMynowski DG and Andersen T (2012b) Suppressing low-order eigenmodes with local control for deformable mirrors. *Optical Engineering* 51(2): 026601–1–026601–9, ISSN 00913286, DOI: 10.1117/1.OE.51.2.026601.

Kopon D, Close LM, Males J, Gasho V and Follette K (2010) The magellan adaptive secondary VisAO camera: Diffraction-limited broadband visible imaging and 20mas fiber array IFU. In: Ellerbroek B, Hart M, Hubin N and Wizinowich P (eds) *Adaptive Optics Systems II*, San Diego, California, USA: SPIE, vol. 7736, pp. 77362V–77362V–11, DOI: 10.1117/12.858062.

Kulkarni J, D'Andrea R, Brandl B, Wizinowich P and Bonaccini D (2003) Application of distributed control techniques to the adaptive secondary mirror of Cornell's Large Atacama Telescope. In: *Adaptive Optical System*

Technologies II, Waikoloa, HI, USA: SPIE, vol. 4839, pp. 750–756, DOI: 10.1117/12.459043.

Kwakernaak H and Sivan R (1972) *Linear Optimal Control Systems*. Wiley-Interscience, 1st ed., ISBN 0471511102.

Lublin L and Athans M (2010) Linear quadratic regulator control. In: Levine W (ed) *The Control Systems Handbook, Second Edition*, CRC Press, vol. 20106837, ISBN 978-1-4200-7364-5, 978-1-4200-7365-2, pp. 17–1–17–25.

Manetti M (2011) *High Precision Shape Control of Masssively Actuated, Magnetically Levitated, Secondary Adaptive Mirrors for Extremely Large Telescopes*. PhD Thesis, Politecnico di Milano, Milano, Italy.

Manetti M, Morandini M and Mantegazza P (2010) High precision massive shape control of magnetically levitated adaptive mirrors. *Control Engineering Practice* 18(12): 1386–1398, ISSN 0967-0661, DOI: 10.1016/j.conengprac.2010.07.002.

Manetti M, Morandini M and Mantegazza P (2012a) Servo-fluid-elastic modeling of contactless levitated adaptive secondary mirrors. *Computational Mechanics* 50(1): 85–98, ISSN 0178-7675, 1432-0924, DOI: 10.1007/s00466-011-0676-4.

Manetti M, Morandini M and Mantegazza P (2013) Self-tuning shape control of massively actuated adaptive mirrors. *Control Systems Technology, IEEE Transactions on* PP(99): 1–1, ISSN 1063-6536, DOI: 10.1109/TCST.2013.2267814.

Manetti M, Morandini M, Mantegazza P, Biasi R, Gallieni D and Riccardi A (2012b) Experimental validation of massively actuated deformable adap-

tive mirror numerical models. *Control Engineering Practice* 20(8): 783–791, DOI: 10.1016/j.conengprac.2012.03.018.

Massioni P and Verhaegen M (2009) Distributed control for identical dynamically coupled systems: A decomposition approach. *Automatic Control, IEEE Transactions on* 54(1): 124–135, ISSN 0018-9286, DOI: 10.1109/TAC.2008.2009574.

Meirovitch L (1990) *Dynamics and Control of Structures.* Wiley, ISBN 9780471628583.

Meirovitch L and Baruh H (1985) The implementation of modal filters for control of structures. *Journal of Guidance, Control, and Dynamics* 8(6), DOI: 10.2514/3.20045.

Mercadal M (1991) Homotopy approach to optimal, linear quadratic, fixed architecture compensation. *Journal of Guidance, Control, and Dynamics* 14(6): 1224–1233, ISSN 0731-5090, DOI: 10.2514/3.20778.

Nocedal J and Wright S (2006) *Numerical Optimization.* Springer, ISBN 9780387400655.

Riccardi A, Brusa G, Salinari P, Busoni S, Lardiere O, Ranfagni P, Gallieni D, Biasi R, Andrighettoni M, Miller S and Mantegazza P (2003) Adaptive secondary mirrors for the large binocular telescope. In: *Proceedings SPIE, Astronomical Adaptive Optics Systems and Applications*, San Diego, USA, vol. 5169, pp. 159–168, DOI: 10.1117/12.511374.

Ruppel T (2012) Modeling and control of deformable membrane mirrors. In: Tyson R (ed) *Adaptive Optics Progress*, InTech, ISBN 978-953-51-0894-8, URL http://www.intechopen.com/books/adaptive-optics-progress/modeling-and-control-

Ruppel T, Dong S, Rooms F, Osten W and Sawodny O (2013) Feedforward control of deformable membrane mirrors for adaptive optics. *Control Systems Technology, IEEE Transactions on* 21(3): 579–589, ISSN 1063-6536, DOI: 10.1109/TCST.2012.2186813.

Smith D (2001) Gemini south wind data. http://www.tuc.noao.edu/system/gsmt/studies/.

Stein G and Gorinevsky D (2005) Design of surface shape control for large two-dimensional arrays. *Control Systems Technology, IEEE Transactions on* 13(3): 422–433, ISSN 1063-6536, DOI: 10.1109/TCST.2004.841659.

Wildi FP, Brusa G, Lloyd-Hart M, Close LM and Riccardi A (2003) First light of the 6.5-m MMT adaptive optics system. In: Tyson R and Lloyd-Hart M (eds) *Astronomical Adaptive Optics Systems and Applications*, San Diego, CA, USA: SPIE, vol. 5169, pp. 17–25, DOI: 10.1117/12.507687.